
Article:
Zheng, M., Zhu, Z.Q., Cai, S. et al. (2019) Influence of stator and rotor pole number combinations on the electromagnetic performance of stator slot-opening PM hybrid-excited machine. IEEE Transactions on Magnetics , 55 (5). 8101210. ISSN: 0018-9464

https://doi.org/10.1109/TMAG.2019.2903769

Influence of Stator and Rotor Pole Number Combinations on the Electromagnetic Performance of Stator Slot-opening PM Hybrid-excited Machine

M. Zheng, Z. Q. Zhu, *Fellow, IEEE*, S. Cai, H. Y. Li, and Y. Liu

Department of Electronic and Electrical Engineering, University of Sheffield, Sheffield S1 3JD, U.K.

A new type of three phase stator hybrid excited machine with permanent magnets (PM) located at the slot openings of field winding slots is presented in this paper. It has the advantage of good flux regulation capability due to the field excitation. The machines with different stator/rotor pole combinations, i.e. 6-stator pole-7/8/10/11/13/14-rotor poles, have been comparatively investigated in terms of the open-circuit and on-load characteristics, as well as the influence of DC current and the unbalanced magnetic forces. 2D finite element analysis (FEA) has been employed for analysis and optimization of the machines, together with experimental validation.

***Index Terms*— hybrid excitation, permanent magnet machine, slot and pole number combination, stator hybrid excitation machine, stator slot opening PM machine.**

I. Introduction

Due to the use of both field windings and PMs for excitation, the hybrid excited machines have the synergies of both DC-excited and PM-excited machines. Adding field windings provides an additional degree of freedom to adjust the excitation flux in air-gap and thus can improve the flux regulation capability of the machine by field weakening/strengthening, as well as the machine efficiency by optimizing the field-armature flux ratio [1-4].

Hybrid excited machines can be classified into parallel and series excitation machine topologies [5], [6], while the PM and field excitations can be both on stator or rotor, or separated onto stator and rotor, respectively [7-8]. When the PM and field excitations are both on stator, the machines have the structure of robust rotor without brushes and slip rings, which are similar to the stator PM machines [9-15]. Many of these kinds of machines are directly modified from the switched flux PM machines (SFPMMs) [9], [10], thus can be called hybrid SFPMMs (HSFPMMs). In comparison with SFPMMs, the PM slots or locations of HSFPMMs are slightly modified by: (a) replacing a part of PMs with field windings [9], [10]; (b) placing field windings on stator back-iron [11]. However, the effectiveness of field excitation is limited by high PM reluctance for the type (a) machine, while the type (b) machine may cause a part of PM flux shunted in the stator back iron. In addition, a few other types of HSFPMMs are designed and investigated with the same PM volume of the SFPMMs, e.g. field windings in the same stator slots with armature windings [15] and E-core HSFPMMs [16] in which the field windings are wound around the redundant teeth of an E-core machine [21].

Another type of hybrid excited machine is proposed based on the variable flux machines (VFMs) and wound field synchronous machines (WFSMs), and its PMs are located on the slot opening area [17-19]. This type of hybrid stator slot opening PM machines (HSSPMMs) has higher torque density than WFSMs, and good flux regulation capability due to the paralleled PM and field excitation. The working principle of HSSPMMs is revealed based on the stator slot opening PM machine [17] [20].

This paper proposes a new type of HSSPMMs with double salient structure which can be modified from either WFSM or E-core SFPMM. The feasible stator and rotor pole combinations for this kind of new three phase HSSPMMs are investigated and discussed. The machine topology and the machine operation principle are described in section II. The windings for the machines having 6 stator poles and 7/8/10/11/13/14-rotor poles are shown in section III. Furthermore, the machine optimization conditions and method are presented in section IV. Open-circuit and on-load characteristics, and the influence of DC current and unbalanced magnetic force are investigated in section V. In section VI, the proposed HSSPMM is compared with a benchmark switched reluctance machine (SRM). The FEA predicted back-EMFs and static torques of the HSSPMMs with 7/8/10/11 rotor poles are experimentally validated in section VII.

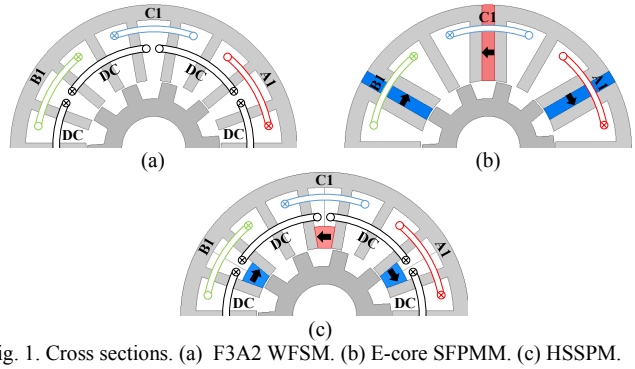

Fig. 1. Cross sections. (a) F3A2 WFSM. (b) E-core SFPMM. (c) HSSPM.

II. Machine Topology and Operation Principle

In this paper, the new type of HSSPMMs, Fig. 1(c), is developed based on the F3A2 WFSM which has coils over three slot pitches for the field windings (F3) and coils over two slot pitches for the armature windings (A2), as shown in Fig. 1(a). The PMs are added and located in the slot openings of the field winding slots of the F3A2 WFSM. The F3A2

HSSPMM can also be derived from the E-core SFPMM, Fig. 1(b), of which the PMs are partly replaced by field windings. The E-core SFPMM is firstly proposed in [21] by removing half of the PMs in the conventional SFPMM and allocating the PMs of opposite polarity between 'E-shaped' stator laminated segments. The coils of the E-core SFPM machine are wound on the stator tooth with PMs inserted [21].

Fig. 2 shows the flux path at open circuit condition for the 11-rotor-pole F3A2 HSSPMM. Without DC current excitation, the PM flux path is shunted in the stator under non-saturated condition and the machine will produce zero open-circuit back-EMF and cogging torque. However, as shown in Fig. 2(a), a few PM flux lines pass to the rotor via the air gap, which means the machine stator is magnetically saturated and exhibits flux leakage. Hence, the open-circuit characteristics such as the back-EMF of the machine without DC field excitation will be non-zero but low. The flux produced by DC current has opposite direction with the stator-shunted PM flux. When the DC current is not over-excited, the stator-shunted PM flux still exists, as shown in Fig. 2(b). When the DC current exceeds the very over-excited value, Fig. 2(c), the machine has no shunted PM flux. Thus, the main purpose of employing field winding in this machine is to push the PM flux to the rotor via air gap, which will definitely enhance the machine performance. Moreover, the DC field excitation can be used to reduce the saturation caused by PM flux.

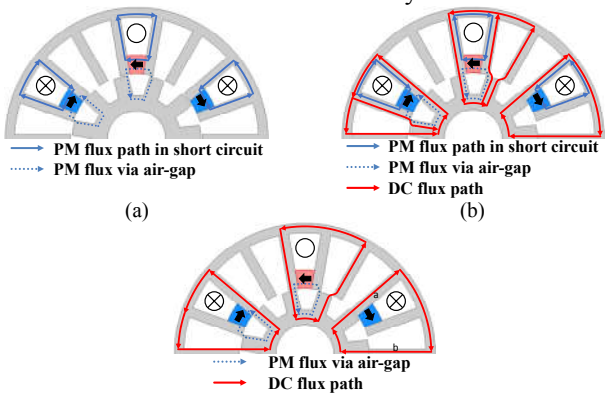

Fig. 2. DC and PM flux paths in half machine models at open-circuit for 11-rotor-pole F3A2 HSSPMM. (a) I_{dc} = 0A. (b) 9A > I_{dc} > 0A. (c) I_{dc} = 9A (machine is over-excited)

III. Stator/Rotor Pole Combinations

Since the F3A2 HSSPM machines can be derived from the E-core SFPM machines, the combinations of stator/rotor pole for the two types of machines can be assumed to be similar. Thus, the feasible stator and rotor pole combinations of an N_{ph} phase F3A2 HSSPM machine are [21]:

$$N_s = k_1 N_{ph}, k_1 = 1, 2, \cdots \quad (1)$$

$$N_r = 2N_s \pm k_2, k_2 = 1, 2 \cdots \quad (2)$$

where N_s and N_r are the numbers of stator and rotor poles respectively, k_1 and k_2 are integers. It should be noted that N_s must be even in order to equip a certain pair of PMs. In this paper, the stator pole number is 6, and according to (2) the rotor pole of the machines are chosen to be 7, 8, 10, 11, 13, and 14.

The fundamental coil back-EMF phasors for the three phase HSSPM machines with 6-7/8/10/11/13/14 stator/rotor poles F3A2 HSSPMMs are shown in Fig. 3. The machine coil back-EMF phasors have two sets of balanced three phase windings with 0 electrical degree phase shift between them. Taking 8-rotor-pole machine as an example, if the coil back-EMF phasor of coil 1 is set as the positive direction, for coils 2, 4 and 6 which are associated with the magnets with opposite magnetization direction, the directions of their coil back-EMF phasors will be opposite and are indicated with ('). Fig. 3(a) shows the schematic of stator armature coil position in mechanical degree for the machines. The corresponding coil back-EMF phasors of the machines with different rotor poles are shown in Fig. 3(b)-(g), respectively.

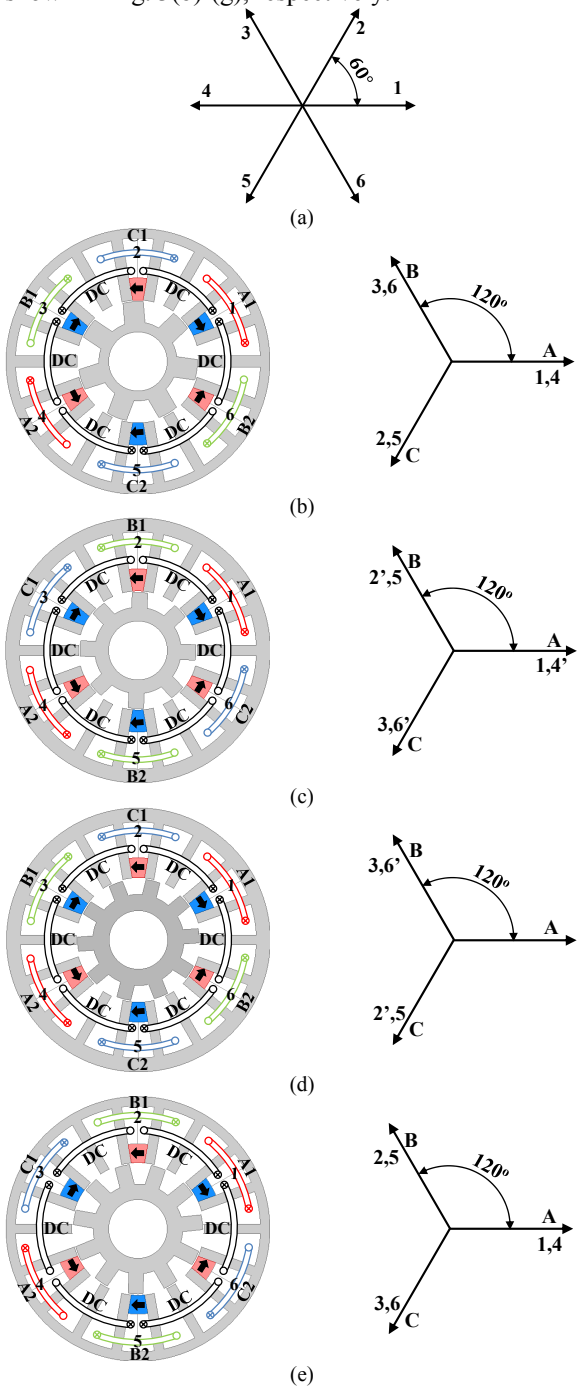

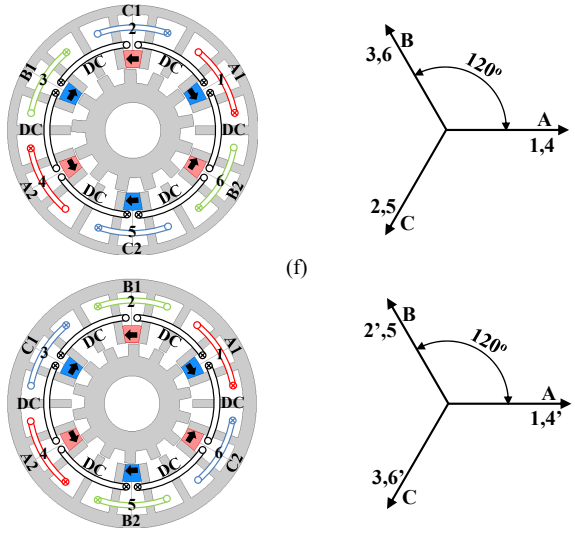

Fig. 3. Winding connections and fundamental back-EMF phasors for F3A2 HSSPMMs with different rotor poles and the cross-sections. (a) Coil position of 6-stator-pole machine (mech. deg.). (b) 7 rotor pole. (c) 8 rotor pole. (d) 10 rotor pole. (e) 11 rotor pole. (f) 13 rotor pole. (g) 14 rotor pole

IV. Machine Optimization

In this section, the F3A2 HSSPMMs are optimized and investigated by using 2D FE method. Genetic algorithm is used to obtain the global optimization of the 7-, 8-. 10-. 11-. 13-, and 14-rotor-pole machines aiming to achieve maximum average electromagnetic torque. To make a fair comparison, some critical parameters need to be fixed during optimization, such as: (a) total copper loss, (b) stator outer radius, (c) air-gap length, (d) stack length, (e) number of turns per phase for armature/field winding, and (f) PM usage. The restrictions for optimization are labelled in Table I, and the geometry parameters are shown in Fig 4. It is worth mentioning that the F3A2 HSSPMMs are optimized based on the F1A1 DL-HSSPMM in [13], of which the number of turns per coil for the armature winding is 46. Since the F1A1 machine in [13] has four coils per phase, while the F3A2 machine in this paper has only two, the number of turns per coil for the armature winding is simply set as 92. In addition, for the F3A2 HSSPM machine, the PMs and field windings are placed in the same slot, making the optimal split of the armature, field winding and PM areas difficult. Thus, for simplicity, the PM volume of the machine is fixed which is similar to the F1A1 DL-HSSPM machine, and the ratio of field current density to armature current density is considered as a variable parameter during the optimization. The parameters to be optimized as well as the optimized values are listed in Table II.

Table I
Restriction for Optimization

Stator outer radius R_{SO}, mm	45
Stack length l_{stack}, mm	25
Air-gap length G, mm	0.5
Shaft radius R_{Rshaft}, mm	10
Total copper loss P_{Cu}, W	60
PM volume V_{PM}, mm^2	5403.8
Pacing factor k_p	0.59
PM N38SH at 20 °C (Br/μr)	1.2T/1.05
Turns per coil (N_a) / total (armature)	92 / 552
Turns per coil (N_f) / total (field)	92 / 552

Table II
Optimized F3A2 HSSPMMs Parameters

	7 pole	8 pole	10 pole	11 pole	13 pole	14 pole
H_{BI}, mm	3.21	4.74	4.77	3.22	3.35	4.79
θ_{st}, mech. deg.	10.33	10.06	8.79	8.56	8.03	7.74
w_{st}, mm	3.75	3.55	3.26	3.37	3.15	2.97
θ_{rt}, mech. deg.	19.75	15.33	13.55	13.17	11.26	10.40
H_{Rtooth},mm	7.16	5.11	5.25	6.86	4.97	4.34
R_{SI}, mm	20.82	20.23	21.25	22.56	22.46	22.00
H_{PM}, mm	7.469	7.474	6.75	6.41	6.23	6.22
J_{ratio}	1.022	1.032	0.935	0.904	0.874	0.667
Total S_a, mm^3	1805.5	1684.7	1700.8	1813.3	1851.1	1722.6
Total S_f, mm^3	1373.4	1252.8	1268.8	1381.2	1419.0	1290.4

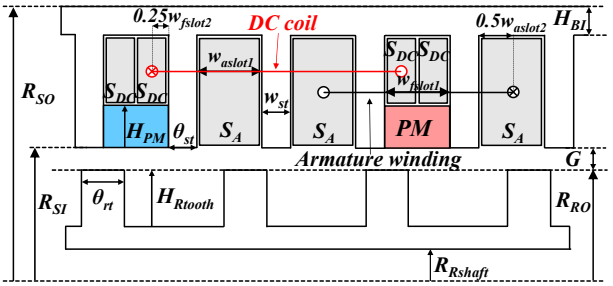

Fig. 4. Illustration of stator and rotor geometric parameters.

The optimization is implemented at a fixed rotor speed of 400 rpm. Since there are two kinds of excitation sources in the proposed machines, the restriction of fixed copper loss in the optimization should be paid special attention. To reduce the quantity of parameters to be optimized, the stator slots for the machines are considered as identical. The slot areas for armature winding (S_a) and field windings (S_f) are different and both are variable during optimization. The armature current density J_a also varies during the optimization, and the field current density J_f can be expressed as J_a multiplied by J_{ratio} (the ratio of field to armature slot current density). The total copper loss of the machines can be calculated by (3) and the current excited in the armature windings I_a and the field windings I_f can be expressed as (4) and (5).

$$P_{Cu} = I_a^2 R_a + I_f^2 R_f \tag{3}$$

$$I_a = \frac{J_a S_a k_p}{N_a} \tag{4}$$

$$I_f = \frac{J_a J_{ratio} S_f k_p}{N_f} \tag{5}$$

where R_a and R_f are the total armature and field winding resistances respectively. The end-winding has been considered in the optimization and the coil end shape is assumed to be rectangle, and hence, the total armature and field end-winding lengths, l_{end_a} and l_{end_f} can be expressed in (6) and (7), respectively.

$$l_{end\_a} = 2\left(\left(\left(S_{SO} - H_{BI}\right) + S_{SI}\right)\pi - 6w_{st}\right) \tag{6}$$

$$l_{end\_f} = 2\left(\left(S_{SO} - H_{BI}\right) + \left(S_{SI} + H_{PM}\right)\right)\pi \tag{7}$$

Thus, the total armature winding resistance and the total field winding resistance are given in (8) and (9), respectively.

$$R_a = \frac{N_a^2 \rho_{Cu}\left(12 l_{stack} + l_{end\_a}\right)}{S_a k_p} \tag{8}$$

$$R_f = \frac{N_f^2 \rho_{Cu} \left(12 l_{stack} + l_{end\_f}\right)}{S_f k_p} \quad (9)$$

where ρ_{Cu} is the electrical resistivity of copper.

V. Electromagnetic Performance

In previous sections, the machine topology, operation principle, the stator/rotor pole combinations of the F3A2 HSSPMs and the machine optimization have been presented. In this section, the machine performance with different rotor poles are investigated and compared.

A. Open-circuit Flux Distribution

The open-circuit flux distribution for the machines with/without DC field excitation are shown in Fig. 5. The flux distributions of the machines without DC field excitation indicate that the flux lines are mainly shunted in the machine stator but a portion of flux circled through air-gap and rotor due to stator saturation. Thus, it can be predicted that the open-circuit characteristics with no DC field winding excitation, e.g. the back-EMF, flux-linkage and cogging torque, of these machines will be non-zero but low at no DC field excitation situation.

B. Open-circuit Flux Linkage

The open-circuit flux linkages of the 6-stator-pole / 7-, 8-, 10-, 11-, 13-, and 14-rotor-pole F3A2 HSSPMMs are shown in Fig. 6. The fundamental phase flux linkage at I_{dc} = 0A is quite small when compared with the corresponding flux enhanced fundamentals with rated DC currents, especially for the 13- and 14- rotor-pole machines. The fundamental flux linkage of the 14-rotor-pole machine has the lowest amplitude and increases slightly when the machine has field excitation whereas for the 7-rotor-pole machine, the magnitude is the highest.

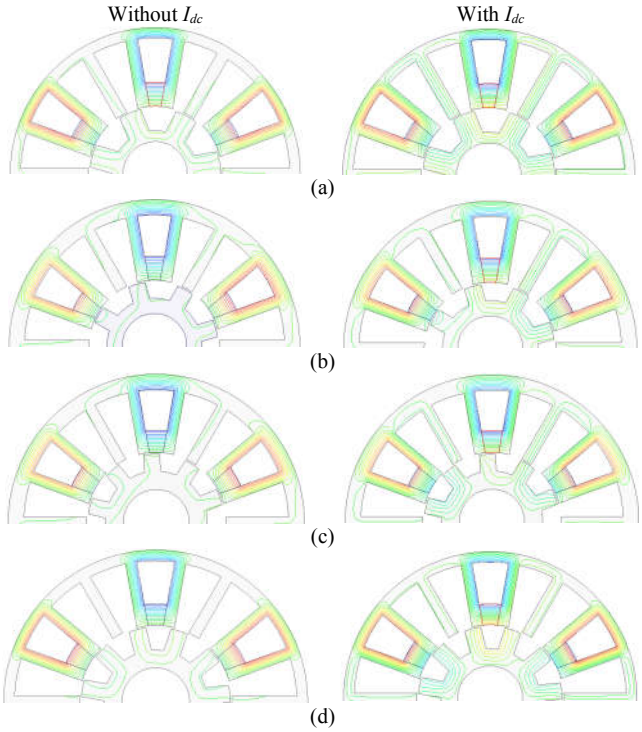

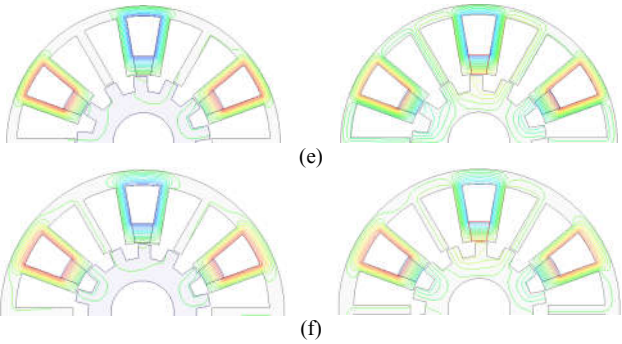

Fig. 5. Open-circuit flux distribution for F3A2 HSSPMMs with different rotor poles. (a) 7 rotor pole. (b) 8 rotor pole. (c) 10 rotor pole. (d) 11 rotor pole. (e) 13 rotor pole. (f) 14 rotor pole.

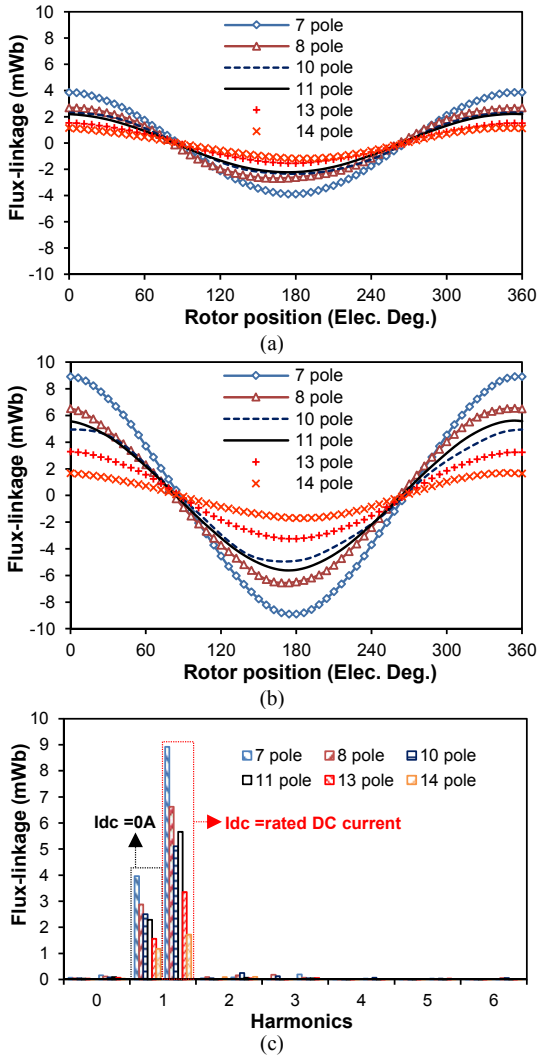

Fig. 6. Open-circuit flux linkages for F3A2 HSSPMMs with different rotor poles (Phase A). (a) Flux linkage waveforms (I_{dc} = 0A). (b) Flux linkage waveforms (rated I_{dc}). (c) Magnitude of harmonics.

C. Open-circuit Back-EMF

The back-EMF comparison is shown in Fig. 7. When the F3A2 HSSPMMs are excited with field excitation, the fundamental harmonics of the back-EMFs are significantly increased when compared with those without field current. The phase back-EMF can be derived from the rate of the change of phase flux-linkage, as [22]:

$$EMF = -\frac{d\psi_{phase}}{dt} \tag{10}$$

$$EMF \propto f\psi_{phase} \tag{11}$$

where ψ_{phase} is the phase flux-linkage, t is the time and f is the frequency.

The 14-rotor-pole machine has the lowest phase back-EMF magnitude due to the low phase flux-linkage, while the 7-rotor-pole machine has the highest. Besides, the machines with even number of rotor poles have asymmetric waveforms which may lead to a large ripple for torque performance.

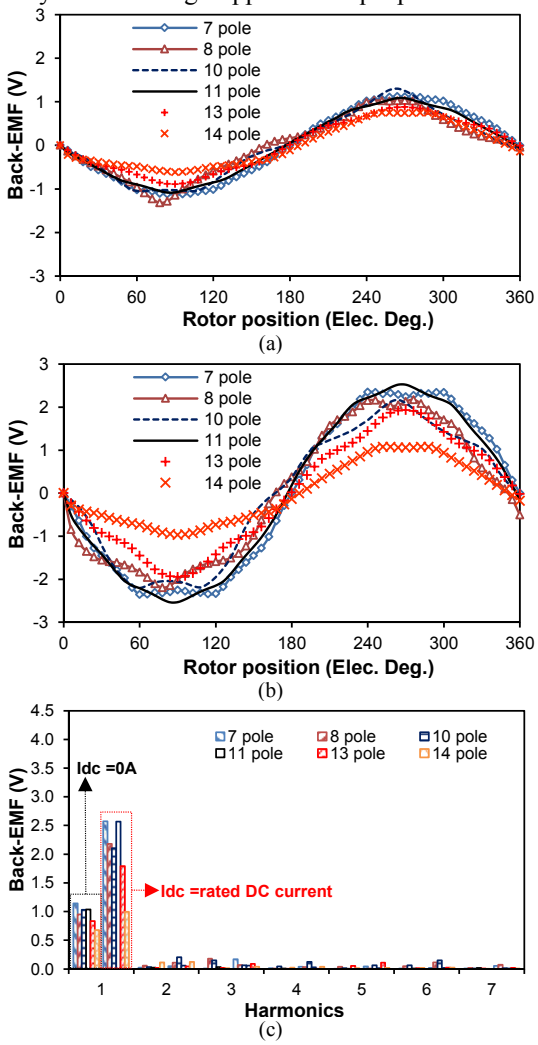

Fig. 7. Open-circuit back-EMFs @ 400 rpm for F3A2 HSSPMMs with different rotor poles (Phase A). (a) Back-EMF waveforms (I_{dc} = 0A). (b) Back-EMF waveforms (rated I_{dc}). (c) Magnitude of harmonics.

D. Influence of DC Current on Back-EMF

Section II has briefly introduced the machine operation principle, and it shows that the machine may be magnetically saturated in stator without current excitation because of the large amount of the PM flux. In addition, magnetic saturation will occur in the machine stator with the increasing DC current due to the machine structure and dual source excitation. In Fig. 8, the open-circuit back-EMF regulation characteristic of the F3A2 HSSPMM having 11 rotor poles is presented. Back-EMF regulation ratio is defined as the ratio of incremental back-EMF and current (the slope of the line shown in Fig. 8). With negative DC excitation, the back-EMF can be reduced although the regulation ratio is limited due to aggravated magnetic saturation. When positive DC is excited, the stator PM flux is pushed to link with rotor and the back-EMF can be enhanced. Since the positive DC excitation tend to alleviate the PM induced magnetic saturation, the back-EMF regulation ratio is higher with positive DC flux-enhancing.

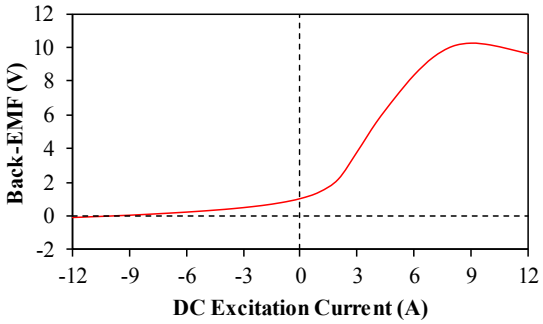

Fig. 8. Open-circuit back-EMF regulation characteristic of F3A2 HSSPMM. (11-rotor poles shown as example)

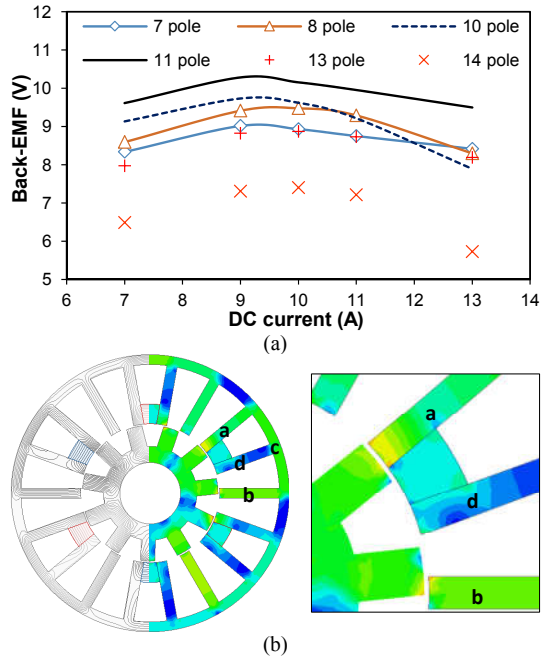

Fig. 9. Influence of the DC field excitation current at open-circuit of F3A2 HSSPMMs with different rotor poles. (a) Back-EMF fundamental harmonic vs. I_{dc} (Phase A). (b) Flux distribution and flux density of the 11-rotor pole machine at I_{dc} = 9A.

To further investigate the influence of DC excitation on the maximum back-EMF, the variation of phase back-EMF of the F3A2 HSSPMMs having different rotor poles with DC current is shown in Fig. 9(a). When the DC currents are around 9A and 10A, the magnitudes of the fundamental phase back-EMF achieve the peak value and then reduce, which means that the machine will be over-excited when the DC current exceeds 10A due to magnetic saturation. The flux distribution at open-circuit, Fig. 9(b), determines that when the magnitude of the phase back-EMF achieves the peak value, the PM flux is not shunted and mainly follow the DC flux path as shown in Fig. 2(c). In that case, the flux density of the machine shows that the stator teeth 'a' and 'b' and the stator back iron 'c' are

suffering severer saturation than the stator tooth 'd'. Meanwhile, the PM is demagnetized at the corners close to the air-gap, and some corners of stator and rotor teeth have high flux density because of the fringing flux.

E. Open-circuit Cogging Torque

Fig. 10 compares the cogging torque. It is found that the F3A2 HSSPMMs with even number of rotor poles have larger open circuit cogging torque compared with odd rotor pole number machines with/without DC excitation conditions. The magnitude of harmonics shows that the even rotor pole number machines have higher 3rd, 6th, 9th and 12th harmonics, while the odd rotor pole number machines only have higher 6th and 12th harmonics but are of much lower magnitudes than those of the even pole machines. The 10-rotor-pole machine has significantly increased 9th harmonic with DC field excitation, which determines the shape of the cogging torque waveform. For the odd rotor pole machines, the magnitudes are increased when DC current is applied. On the contrary, the even rotor pole machines have lower magnitude with the DC field excitation.

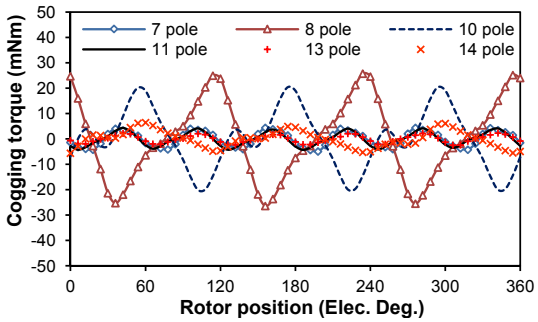

(a)

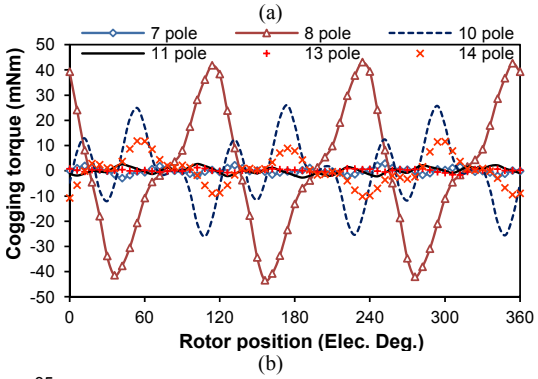

(b)

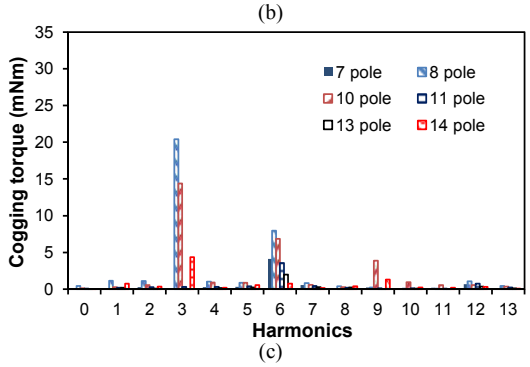

(c)

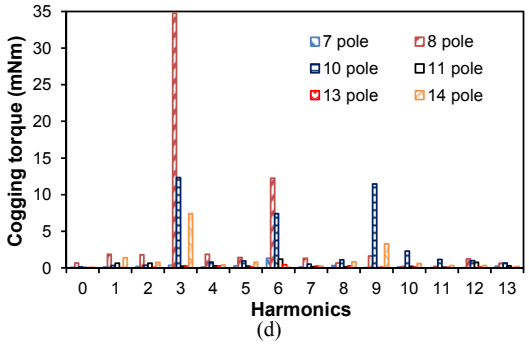

(d)

Fig. 10. Open-circuit cogging torques for F3A2 HSSPMMs with different rotor poles. (a) Cogging torque waveforms (I_{dc} = 0A). (b) Cogging torque waveforms (rated I_{dc}). (c) Magnitude of harmonics (I_{dc} = 0A). (d) Magnitude of harmonics (rated I_{dc}).

F. On-load Electromagnetic Performance

The current angle for the machines should be analyzed to ensure the maximum average electromagnetic torque during the machine optimization. The average torques against current angle are shown in Fig. 11. As can be seen, the machines can achieve the maximum average torque within 0 to 10 electrical degree current angle. This proves that the machines have small or negligible reluctance torque.

With total copper loss of 60W and optimal current angle, the electromagnetic torques of the F3A2 HSSPMMs are shown in Fig. 12. Fig. 12(a) shows that the even rotor pole machines have large torque ripple and the 14-rotor pole machine has the worse torque performance because of the lowest amplitude of the back-EMF and asymmetric waveform. Apart from the fundamental harmonic, the odd rotor pole machines only have the 6th harmonic, while the even rotor pole machines have an additional 3rd harmonic which causes the large torque ripple. For the 14-rotor pole machine, the 3rd harmonic is the largest, and thus, the torque ripple for the machine is the largest. Meanwhile, the 11-rotor-pole machine has the lowest toque ripple together with the highest average torque.

The average toque rises with the increasing total copper loss, and it shows that the machines will be saturated at high copper loss, as shown in Fig. 13. The 14-rotor-pole machine has the lowest average torque within the whole copper loss region, and the 11-rotor-pole machine has the highest average toque. The 7- and 10-rotor-pole machines and the 8- and 13-rotor-pole machines have similar average torque values at low copper loss. However, when the copper loss is high, the 7- and 13-rotor-pole machines have lower average torque than the 8- and 10-rotor pole machines.

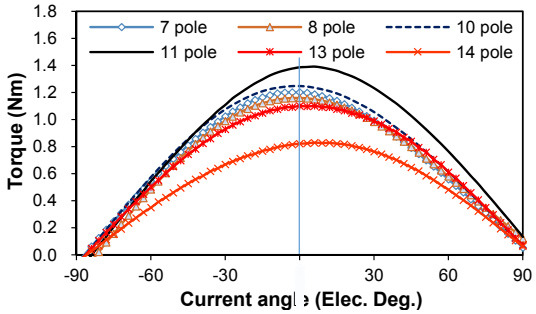

Fig. 11. Electromagnetic torque against current angle for F3A2 HSSPMMs with different rotor poles (total copper loss = 60W).

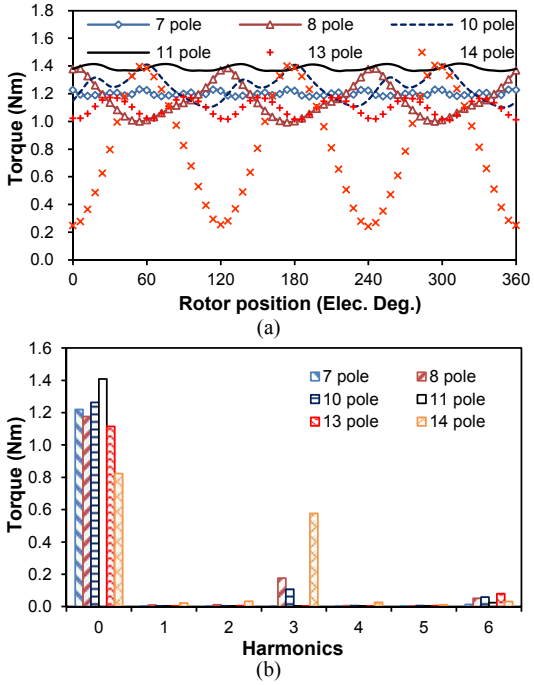

Fig. 12. Electromagnetic torques for F3A2 HSSPMMs with different rotor poles (total copper loss = 60W). (a) Electromagnetic torque waveforms. (b) Magnitude of harmonics.

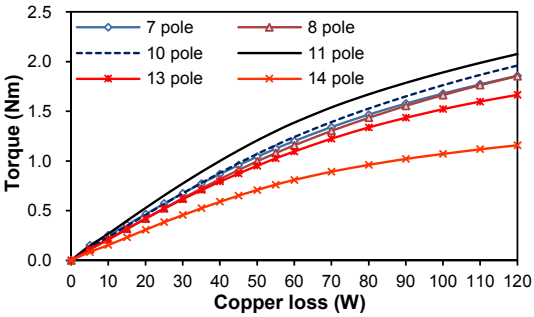

Fig. 13. Average electromagnetic torque against total copper loss for F3A2 HSSPMMs with different rotor poles.

G. Unbalanced Magnetic Force

The unbalanced magnetic force (UMF) can be calculated from the tangential and radial magnetic forces. Both tangential and radial magnetic forces can be transformed into x- and y-axes, F_x and F_y as:

$$F_x = F_{tx} + F_{rx} = \frac{rl_{stack}}{2\mu_0}\int_0^{2\pi}\left(2B_rB_\alpha\sin\alpha + \left(B_\alpha^{\,2} - B_r^{\,2}\right)\cos\alpha\right)d\alpha \quad (12)$$

$$F_y = F_{ty} + F_{ry} = \frac{rl_{stack}}{2\mu_0}\int_0^{2\pi}\left(-2B_rB_\alpha\sin\alpha + \left(B_\alpha^{\,2} - B_r^{\,2}\right)\cos\alpha\right)d\alpha \quad (13)$$

where F_{tx}, F_{ty}, F_{rx} and F_{ry} are the xy-axis components of tangential and radial magnetic forces, respectively. B_α and B_r are the circumferential and radial components of the air gap flux density, respectively, r is the air gap radius, and μ_0 is the permeability of the free space [23].

Fig. 14(a) and (b) show the UMF loci with/without DC field current at on-load situation for the F3A2 HSSPMMs with different rotor poles. It shows that the odd rotor pole number machines exhibit UMF, while the machines with even rotor pole have negligible UMF. The UMF is caused by the difference in the air-gap flux densities on opposite sides of a machine, as displayed by the flux line distributions and clearly the odd number rotor pole machines are unbalanced.

Machine total UMF can be calculated as:

$$F = \sqrt{F_x^{\,2} + F_y^{\,2}} \quad (14)$$

The peak UMF for the machines will increase with DC field excitation. Especially for the 11-rotor-pole machine, the peak force is increased by 20% when DC field excited current is increased from zero to the rated value. The peak UMF without DC field current increases slightly with the increasing number of rotor poles. However, the peak UMF for 11-rotor-pole machine is the largest when the machines have DC field current.

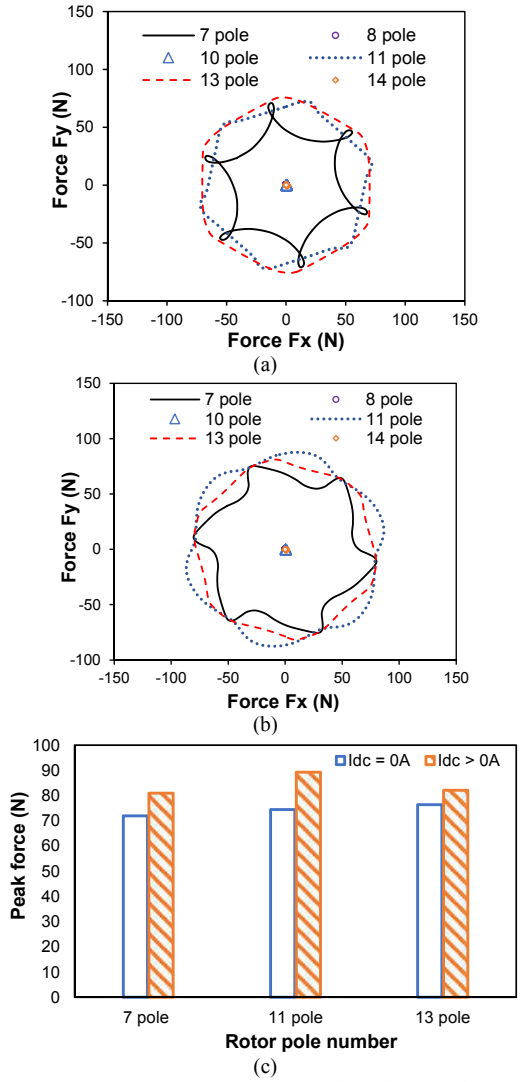

Fig. 14. UMFs for F3A2 HSSPMMs at on-load (total copper loss = 60W). (a) UMF loci at on-load situation without I_{dc}. (b) UMF loci at on-load situation with rated I_{dc}. (c) Peak force for different rotor poles with and without I_{dc}.

VI. Performance Comparison

To evaluate the output capability of the proposed F3A2 HSSPMM, a conventional doubly salient machine, viz. switched reluctance machine (SRM) is optimized as the benchmark. The optimization process of the SRM is the same as the discussion in section IV to gain a fair comparison, and the SRM is driven within square current of θ_e=(0, 120°). After

global optimization, the main dimensional parameters of the SRM are listed in TABLE III.

Table III

GLOBALLY OPTIMIZED PARAMETERS OF SRM

Parameters	Unit	SRM
Stator slots	-	6
Rotor poles	-	4
Split ratio	-	0.55
Stator yoke thickness	mm	5.9
Stator tooth width	mm	10.6
Rotor tooth width	mm	10.2
Rotor tooth height	mm	4.5

When only phase-A is excited, the flux line and flux density distribution of the SRM are illustrated in Fig. 15, with aligned and unaligned rotor position, respectively. It can be identified that the phase A flux linkage at aligned position is distinctively larger than that at unaligned position, being 0.001Wb/turn and 0.0005Wb/turn, respectively. The different energy storages at aligned and unaligned positions contribute to the torque production of SRM with corresponding current excitation.

As discussed in section V, the torque density of F3A2 HSSPMM with 11-rotor pole is superior to the other counterparts. Therefore, the HSSPMM with 11-rotor pole is chosen to compare with the optimized SRM under the same total copper loss.

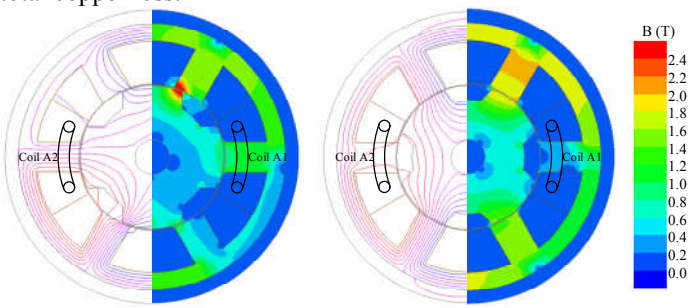

(a) (b)

Fig. 15. Flux line and flux density distribution when only phase-A is excited. (a) Rotor tooth is aligned with phase-A axis. (b) Rotor tooth is unaligned with phase-A axis.

The variations of phase flux linkage with phase current of the SRM and the proposed HSSPMM are shown in Fig. 16. For the SRM, the flux linkages as well as energy storages at aligned and unaligned position are different with single phase excitation. Nevertheless, the phase flux linkages for the proposed HSSPMM without DC and PM at aligned and unaligned position are similar when phase current is excited only. When DC and PM are excited, the flux linkages at aligned and unaligned position are different due to PM and field excitation.

It should be noted the different phase flux linkages for SRM are caused by phase current excitation and reluctance variation. The flux at aligned and unaligned positions are unipolar as shown in Fig. 16. Therefore, unipolar current is preferred for the conventional SRM and the machine can rotate due to the energy conversion. However, the flux linkage differences of the proposed HSSPMM at aligned and unaligned position are due to the interaction of stator PM and DC excitation with rotor reluctance variation. Subsequently, the proposed HSSPMM is more similar with the PM synchronous machine and bipolar current is injected.

Although the SRM has higher energy difference from aligned position to unaligned position compared with the proposed HSSPMM, as shown in Fig. 16, the phase current excitation is unipolar. Therefore, the torque density of the proposed HSSPMM with the SRM will be further illustrated as follows.

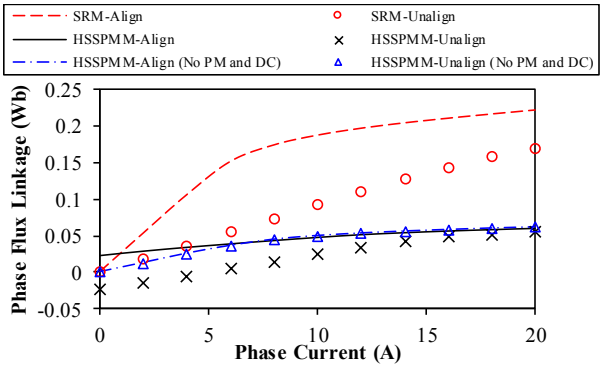

Fig. 16. Variations of phase flux linkage with phase current with single phase excited.

With total copper loss of 60W and optimal current angle, the electromagnetic torques for the SRM and the 11-rotor pole F3A2 HSSPMMs with/without PM are shown in Fig. 17. The existence of PM alleviates the magnetic saturation and improves the torque density. Besides, the torque density of the HSSPMM with PM is similar with the SRM, being 1.39 Nm and 1.36 Nm, respectively. However, the torque ripple of the HSSPMM (3.8%) is significantly smaller than that of SRM (172%).

In order to evaluate the overload capability, the average torques of the SRM and the HSSPMM against copper loss are further compared in Fig. 18. The benefit of employing slot PM can be identified especially with over-load operation. The stator slot PM reduces the magnetic saturation caused by field and armature current, consequently, pulling up the knee point. The average torque of the HSSPMM is similar with the SRM with relatively low copper loss. However, the HSSPMM exhibits slightly better over-load capability than the SRM since the slot PM mitigates the magnetic saturation at heavy load.

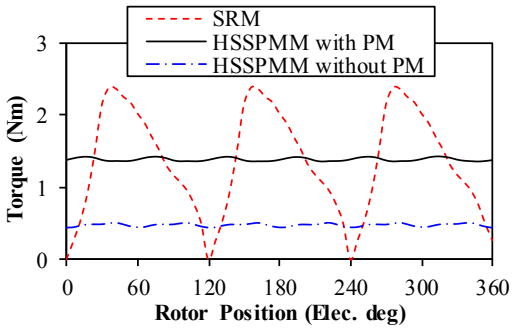

Fig. 17. Electromagnetic torque comparisons for SRM and F3A2 HSSPMMs with/without PM (total copper loss = 60W).

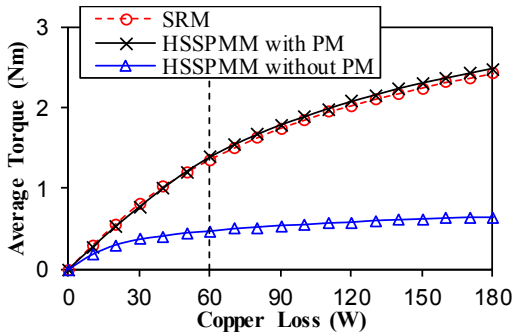

Fig. 18. Average torque against total copper loss for SRM and F3A2 HSSPMMs with/without PM.

VII. Experimental Validation

The prototypes of F3A2 HSSPMMs with 7/8/10/11 rotor poles are shown in Fig. 19. The machine prototypes have been optimized with the total copper loss of 30W and a packing factor of 0.4. The stator of the machines for different stator/rotor pole combinations is designed to be identical, and thus, the design parameters are only considered to be the rotor pole arc and rotor tooth height. The design parameters are given in Table IV.

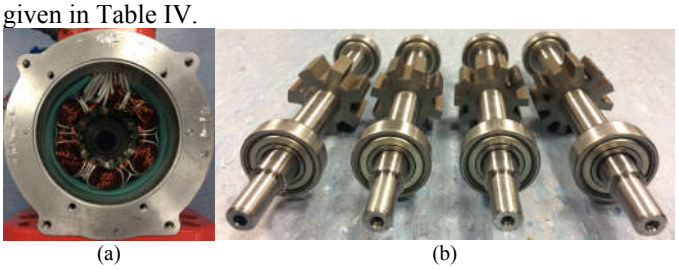

(a) (b)

Fig. 19. Prototype F3A2 HSSPMMs. (a) stator. (b) 7/8/10/11 rotor poles.

Table IV
Optimized Parameters for Machine Prototypes

	7 poles	8 poles	10 poles	11 poles
R_{SO}, mm	45			
l_{Stack}, mm	25			
G, mm	0.5			
θ_{st}, mech. deg.	8.93			
P_{Cu}, W	30			
k_p	0.4			
Split ratio (R_{SI}/R_{SO})	0.477			
N_a/N_f	46/46			
H_{PM}, mm	6.66			
Rotor speed, rpm	400			
Rated current, A	2.51			
Rated current density, A/mm^2	5			
θ_{rt}, mech. deg.	20.95	15.96	12.94	12.96
H_{Rtooth}, mm	7.51	6.74	7.54	7.00
J_{ratio}	0.90	1.07	1.07	0.94

The measured and 2D FEA predicted back-EMF and static torque waveforms of the 6-7/8/10/11 stator/rotor pole F3A2 HSSPMMs are shown in Fig. 20 and Fig. 21, respectively. The back-EMFs are predicted and measured with rated DC current density of 5 A/mm^2. Good agreement between the FEA predicted and measured results has been obtained. The machines with even number of rotor poles have asymmetric back-EMF waveforms as predicted. The static torques are measured under the field and armature (peak value) current densities of 0, 2, 4, and 6A/mm^2. The static torque waveforms at rated current density is shown in Fig. 21(a). During the tests, the three phase armature windings are excited with DC current as I_a=-2I_b=-2I_c. Generally, good agreement is achieved between the measured and predicted static torques, as shown in Fig. 21. The static torques of the 11-rotor-pole machine remain the highest while those of the 8-rotor-pole machine remain the lowest regardless of the current density. Similar to the back-EMF waveforms, the machines with even rotor pole numbers have non-symmetrical static torque waveforms. Meanwhile, with the increasing current density, the differences between the measured and predicted values increase for both back-EMF and static torque.

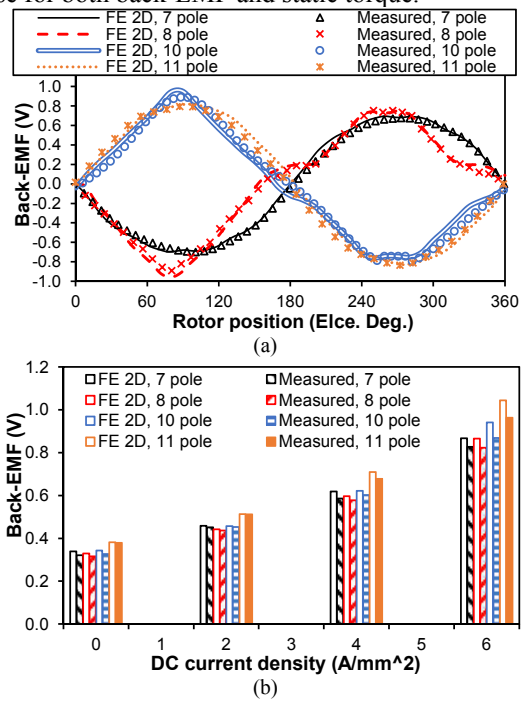

Fig. 20. Open-circuit back-EMF @ 400 rpm of F3A2 HSSPMMs with different rotor poles. (a) Back-EMF waveforms at rated DC current density of 5A/mm^2. (b) Magnitude of back-EMF waveforms at different DC current densities.

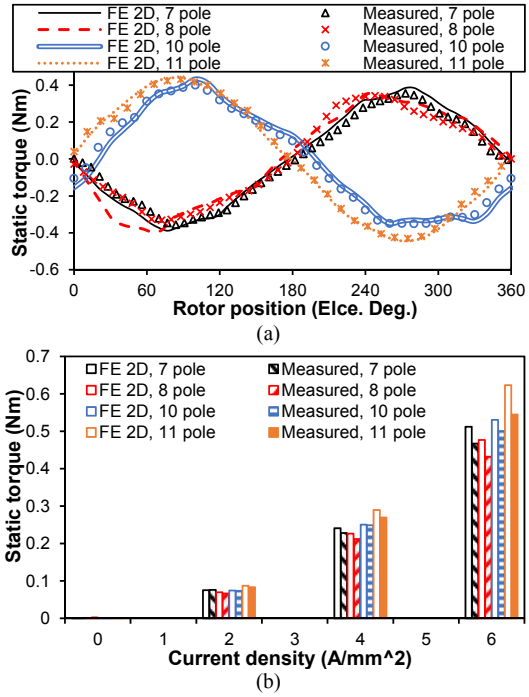

Fig. 21. Static torque of F3A2 HSSPMMs with different rotor poles. (a) Static torque waveforms at rated current density of 5A/mm^2. (b) Magnitude of static torque waveforms at different DC current densities.

VIII. Conclusion

In this paper, the open-circuit and on-load electromagnetic performance of the 18-stator slot F3A2 HSSPMMs with 7/8/10/11/13/14-rotor poles are investigated and compared. The 14-rotor-pole machine has the worst performance in terms of torque and torque ripple, whereas those of the 11-rotor-pole machine are the best. According to the back-EMF waveforms, the even rotor pole machines have asymmetric waveforms due to higher order even harmonics, and hence produce high torque ripple. In addition, the UMFs of the odd rotor pole machines are larger especially when the machines have DC field excitation and the 11-rotor pole machine exhibits the largest UMF value. Compared with conventional doubly salient structure, viz. SRM, the torque density of proposed HSSPMM is similar whereas the torque ripple is mitigated significantly.

References

[1] J. F. Gieras, "PM synchronous generators with hybrid excitation systems and voltage control capabilities: a review," in *Proc. of the Int. Conf. Electr. Mach, ICEM 2012, Marseille, France, Sept. 2-5, 2012*. pp. 2573-2579.

[2] B. Nedjar, S. Hlioui, Y. Amara, L. Vido, M. Gabsi and M. Lecrivain, "A New Parallel Double Excitation Synchronous Machine," *IEEE Trans. on Magn.*, vol. 47, no. 9, pp. 2252-2260, Sept. 2011.

[3] Z. R. Zhang, Y. G. Yan, S. S. Yang and Z. Bo, "Principle of Operation and Feature Investigation of a New Topology of Hybrid Excitation Synchronous Machine," *IEEE Trans. on Magn.*, vol. 44, no. 9, pp. 2174-2180, Sept. 2008.

[4] P. D. Barba, M. Bonislawski, R. Palka, P. Paplicki and M. Wardach, "Design of Hybrid Excited Synchronous Machine for Electrical Vehicles," *IEEE Trans. on Magn.*, vol. 51, no. 8, pp. 1-6, Aug. 2015.

[5] B. N. Naoe, and T. Fukami "Trial production of a hybrid excitation type synchronous machine," *Int. Electr. Machines and Drives Conf. IEMDC 2001, Boston, MA, 2001*. pp. 545 – 547.

[6] Y. Wang and Z. Q. Deng, "Comparison of Hybrid Excitation Topologies for Flux-Switching Machines," *IEEE Trans. on Magn.*, vol. 48, no. 9, pp. 2518-2527, Sept. 2012.

[7] X. Luo and T. A. Lipo, "A synchronous/permanent magnet hybrid AC machine," *IEEE Trans. Energy Convers.*, vol. 15, no. 2, pp. 203–210, Jun. 2000.

[8] J. A. Tapia, F. Leonardi, and T. A. Lipo, "Consequent-pole permanentmagnet machine with extended field-weakening capability," *IEEE Trans. Ind. Appl.*, vol. 39, no. 6, pp. 1704–1709, Nov./Dec. 2003.

[9] W. Hua, M. Cheng, and G. Zhang, "A novel hybrid excitation flux-switching motor for hybrid vehicles," *IEEE Trans. on Magn.*, vol. 45, no.10, pp. 4728-4731, Oct. 2009.

[10] R. L. Owen, Z. Q. Zhu, and G. W. Jewell, "Hybrid-excited flux-switching permanent-magnet machines with iron flux bridges" *IEEE Trans. on Magn.*, vol. 46, no. 6, June 2010, pp.1726-1729.

[11] E. Sulaiman, T. Kosaka and N. Matsui, "High Power Density Design of 6-Slot–8-Pole Hybrid Excitation Flux Switching Machine for Hybrid Electric Vehicles," *IEEE Trans. on Magn.*, vol. 47, no. 10, pp. 4453-4456, Oct. 2011.

[12] C. H. Liu, K. T. Chau, J. Z. Jiang and S. X. Niu, "Comparison of Stator-Permanent-Magnet Brushless Machines," *IEEE Trans. on Magn.*, vol. 44, no. 11, pp. 4405-4408, Nov. 2008.

[13] H. Hua and Z. Q. Zhu, "Novel Hybrid-Excited Switched-Flux Machine Having Separate Field Winding Stator," *IEEE Trans. on Magn.*, vol. 52, no. 7, pp. 1-4, July 2016.

[14] W. Xu and M. He, "Novel 6/7 Stator/Rotor Hybrid Excitation Doubly Salient Permanent Magnet Machine," *IEEE Trans. on Magn.*, vol. 52, no. 7, pp. 1-5, July 2016.

[15] B. Gaussens, E. Hoang, M. Lecrivain, P. Manfe, and M. Gabsi, "A hybrid excited flux-switching machine for high-speed DC-alternator applications," *IEEE Trans. on Ind. Electronics*, vol. 61, no.6, pp. 2976-2989, 2014.

[16] J. T. Chen, Z. Q. Zhu, S. Iwasaki, and R. P. Deodhar, "A novel hybrid-excited switched-flux brushless AC machine for EV/HEV applications" *IEEE Trans. on Vehicular Technology*, vol. 60, no. 4, pp.1365-1373, May 2011.

[17] I. A. A. Afinowi, Z. Q. Zhu, Y. Guan, J. C. Mipo, and P. Farah, "Hybrid-excited doubly salient synchronous machine with permanent magnets between adjacent salient stator poles," *IEEE Trans. on Magn.*, vol. 51, no. 10, October 2015.

[18] Z. Q. Zhu, I. A. A. Afinowi, Y. Guan, J. C. Mipo, and P. Farah, "Hybrid-excited stator slot permanent magnet machines—influence of stator and rotor pole combinations," *IEEE Trans. on Magn.*, vol. 52, no. 2, February 2016.

[19] H. Nakane, T. Kosaka, and N. Matsui, "Design studies on hybrid excitation flux switching motor with high power and torque densities for HEV applications," *IEEE Int. Electric Machines & Drives Conference, IEMDC 2015, Coeur d'Alene, ID, USA, May 10-13, 2015*. pp: 234-239.

[20] K. Nakamura, K. Murota, and O. Ichinokura, "Characteristics of a novel switched reluctance motor having permanent magnets between the stator pole-tips," *European Conf. on Power Electronics and Applications 2007, Aalborg, Denmark, Sept. 2-5, 2007*. pp: 1-5.

[21] J. T. Chen, Z. Q. Zhu, S. Iwasaki, and Rajesh P. Deodhar, "A novel E-core switched-flux PM brushless AC machine," *IEEE Trans. on Ind. Electronics*, vol. 47, no. 3, pp: 1273-1282, May/June 2011.

[22] D. Ishak, Z. Q. Zhu, and D. Howe, "Comparison of PM brushless motor. Having either all teeth or alternate teeth wound," *IEEE Trans. on Energy Conversion.*, vol. 21, no. 1, pp: 95-103, March 2006.

[23] J. T. Chen, and Z. Q. Zhu, "Comparison of all- and alternate-poles-wound flux-switching PM machines having differnet stator and rotor pole numbers," *IEEE Trans. on Ind. Appl.*, vol. 46, no. 4, pp: 1406-1415, July/Aug. 2010.